Prompt Gamma Ray Burst emission from gradual magnetic dissipation

Paz Beniamini, Dimitrios Giannios

Monthly Notices
of the
ROYAL ASTRONOMICAL SOCIETY

MNRAS **468,** 3202–3211 (2017)
Advance Access publication 2017 March 23

doi:10.1093/mnras/stx717

Prompt gamma-ray burst emission from gradual magnetic dissipation

Paz Beniamini[1,2]★ and Dimitrios Giannios[3]

[1]*Institut d'Astrophysique de Paris UMR 7095 Université Pierre et Marie Curie-Paris 06; CNRS 98 bis bd Arago, F-75014 Paris, France*
[2]*Department of Physics, The George Washington University, Washington, DC 20052, USA*
[3]*Department of Physics and Astronomy, Purdue University, 525 Northwestern Avenue, West Lafayette, IN 47907, USA*

Accepted 2017 March 21. Received 2017 March 21; in original form 2016 December 19

ABSTRACT

We considered a model for the prompt phase of gamma-ray burst emission arising from a magnetized jet undergoing gradual energy dissipation due to magnetic reconnection. The dissipated magnetic energy is translated to bulk kinetic energy and to acceleration of particles. The energy in these particles is released via synchrotron radiation as they gyrate around the strong magnetic fields in the jet. At small radii, the optical depth is large, and the radiation is reprocessed through Comptonization into a narrow, strongly peaked component. At larger distances the optical depth becomes small and radiation escapes the jet with a non-thermal distribution. The obtained spectra typically peak around ≈300 keV (as observed) and with spectral indices below and above the peak that are, for a broad range of the model parameters, close to the observed values. The small radius of dissipation causes the emission to become self-absorbed at a few keV and can sufficiently suppress the optical and X-ray fluxes within the limits required by observations .

Key words: magnetic reconnection – radiation mechanisms: non-thermal – radiation mechanisms: thermal – gamma-ray burst: general.

1 INTRODUCTION

Relativistic Poynting-flux-dominated jets have been suggested to occur in various astrophysical outflows, including active galactic nuclei (AGNs), pulsars, micro-quasars and gamma-ray bursts (GRBs). The alternative situation that the jet is accelerated through thermal pressure gradients has been ruled out for AGNs, based on the available thermal power at the jet's base (Ghisellini & Tavecchio 2009). This suggests that magnetic jets dominate those environments and indeed may be universal, thus encouraging us to consider the possibility of magnetic jets operating in GRBs as well (see also Leng & Giannios 2014). Furthermore, magnetic jets in GRBs are supported based on modelling of the accretion disc (Kawanaka, Piran & Krolik 2013).

The emission process in prompt GRBs is highly debated. The overall non-thermal spectrum has led to the suggestion that the radiation is dominated by synchrotron emission from a power-law distribution of electrons (Katz 1994; Rees & Meszaros 1994; Sari, Narayan & Piran 1996; Sari, Piran & Narayan 1998; Kumar & McMahon 2008; Daigne, Bošnjak & Dubus 2011; Beniamini & Piran 2013). A major concern for this model regards the low-energy spectral slope. The synchrotron fast cooling (which is the required cooling regime for obtaining large radiative efficiencies) photon index below the peak, $\mathrm{d}N/\mathrm{d}\nu \equiv N_\nu \propto \nu^\alpha$, is $\alpha = -1.5$ and is inconsistent with the typically observed slope of $\alpha = -1$. Although it is relatively easy to achieve softer spectra $\alpha < -1.5$, it is extremely difficult to increase α in these models.[1] However, 90 per cent of all GRBs have $\alpha > -1.5$ (Preece et al. 2000; Ghirlanda, Celotti & Ghisellini 2002; Kaneko et al. 2006; Nava et al. 2011) and ≈40 per cent of GRBs have $\alpha > -2/3$ (Nava et al. 2011), which is impossible for optically thin synchrotron, even in the slow cooling regime. This problem is referred to as the synchrotron 'line of death' (Preece et al. 1998). Other problems with a synchrotron origin for the prompt phase involve the narrow peak energy distribution and the apparent sharp decline of the peak energy distribution above 1 MeV (Band et al. 1993; Mallozzi et al. 1995; Schaefer 2003; Beloborodov 2013), although this could also be due to a selection effect (Shahmoradi & Nemiroff 2010; Beniamini & Piran 2013) and the narrow spectral width of the observed 'band function' as compared with the synchrotron peak (Baring & Braby 2004; Burgess et al. 2011; Daigne et al. 2011; Beloborodov 2013; Yu et al. 2016). The main alternative to synchrotron is photospheric emission. The photospheric emission component can be powerful. It is characterized by hard low-energy spectral slopes and, provided that there is energy dissipation close to the photosphere, a broader spectrum that resembles the observed one (Goodman 1986; Thompson 1994; Mészáros & Rees 2000; Giannios 2006; Beloborodov 2010;

★ E-mail: paz.beniamini@gmail.com

[1] Inverse Compton (IC) cooling in the Klein–Nishina (KN) regime could help to increase somewhat the low-energy synchrotron spectral slope. At best, if only a small fraction of the electrons are accelerated, the slope could approach $\alpha \to -1$ (Daigne et al. 2011).

Lazzati & Begelman 2010; Giannios 2012). Photospheric emission models have their own share of problems, such as the need for a significant amount of dissipation and non-thermal acceleration deep below the photosphere (Vurm, Lyubarsky & Piran 2013) and various GRBs in which strong limits have been put on the thermal component (Ryde & Pe'er 2009; Ryde et al. 2010; Guiriec et al. 2011, 2013; Axelsson et al. 2012).

In magnetic jets, the outflow may be composed of wound-up magnetic field lines in a 'striped wind' configuration (Coroniti 1990; Spruit, Daigne & Drenkhahn 2001), in which their polarity is reversed over a typical distance λ. Reconnection is then the most efficient process for dissipating the magnetic energy and transferring it to the emitting particles (Spruit et al. 2001; Drenkhahn & Spruit 2002). Many studies (Giannios 2008; Zhang & Yan 2011; McKinney & Uzdensky 2012; Sironi, Petropoulou & Giannios 2015; Beniamini & Granot 2016; Granot 2016; Kagan, Nakar & Piran 2016; Bégué Peèr & Lyubarsky 2017) have therefore recently considered reconnection models as strong candidates for reproducing the prompt sub-MeV emission. In MHD jets, the energy dissipation through reconnection occurs gradually over a wide range of radii (Drenkhahn 2002). At small radii, the jet is optically thick and photons produced via synchrotron emission are thermalized, leading to, to a zeroth approximation, a blackbody-like signature from the photosphere (Giannios & Spruit 2005). Assuming that the dissipated energy smoothly heats the flow (e.g. a slow-heating scenario following Ghisellini & Celotti 1999), Giannios (2006) showed that Comptonization close to the photosphere distorts the spectrum resulting in a high-energy power-law tail. At larger radii, the radiation is dominated by synchrotron emission, and the typical frequencies and fluxes evolve as a function of the magnetization, dissipation rate, etc. The emitted radiation SED from both the $\tau \sim 1$ surface and the optically thin parts of the jet sensitively depends, however, on the assumptions of the injected particle spectrum at various scales in the jet.

Recent progress in understanding the non-thermal processes at the reconnection layer allow us to revisit this problem. In particular, recent particle-in-cell (PIC) simulations have demonstrated that magnetic reconnection in a high-magnetization σ (where σ is the ratio of the Poynting flux to kinetic luminosities) plasma results in extended, power-law particle distribution. The particle power-law index depends sensitively on σ and the particle spectra become softer for lower σ (e.g. Cerutti et al. 2012; Sironi & Spitkovsky 2014; Guo et al. 2014; Melzani et al. 2014; Lloyd-Ronning & Fryer 2016; Sironi, Giannios & Petropoulou 2016). These studies make specific predictions on the distribution of the accelerated particles expected at different scales in the jet.

Previous works have focused on one or just a few of these various ingredients. In this work, we combine the MHD dynamics, the details of the dissipation process as implied by the new results from PIC simulations and a simple calculation for the emerging emission within a self-consistent model. This model has a rather small number of free parameters: the jet luminosity, L, the 'wavelength' of the structured magnetic field in the jet over the outflow velocity from the reconnection sites, λ/ϵ, the initial total energy per Baryon, η, and the fraction of accelerated electrons, ξ. The dynamical ranges of these parameters are expected to be quite small. It is naturally expected to result in spectra peaking around $\approx$300 keV (as observed) and with spectral indices that closely match the observed values. In addition, the small radius of dissipation causes the spectrum to become self-absorbed at a few keV and can sufficiently suppress the optical and X-ray fluxes below the upper limits required by observations (Beniamini & Piran 2014).

2 MODEL DESCRIPTION

2.1 Dynamics

We consider a Poynting-flux-dominated outflow that is composed of a 'striped wind' magnetic field configuration (Coroniti 1990; Spruit et al. 2001), in which the typical 'wavelength' of the field is λ. Such a configuration can be expected either if the central engine is a non-axisymmetric rotating millisecond magnetar or if it is an accreting black hole (BH). In the millisecond magnetar model, the scale of the stripe, λ, is related to the frequency of the rotator $\lambda \sim \pi c/\Omega \sim 10^8$ cm. For an accreting BH, where the magnetic field that is advected inwards with the flow randomly switches sign (e.g. due to an instability in the disc or accretion of different blobs of plasma with randomly oriented frozen-in field lines), λ/c corresponds to the time-scale to accrete a blob that forms close to the inner edge of the disc. Recent simulations of magnetic jets powered by BH accretion discs provide motivation that the jet may be highly variable on time-scales: $10 - 10^3 r_g/c$ (e.g. Parfrey, Giannios & Beloborodov 2015), where $r_g = GM/c^2$. Therefore, the length-scale $\lambda = 10^7 - 10^9$ cm is typical for both GRB central engine models.

As the flow propagates, magnetic energy is dissipated via reconnection of oppositely oriented field lines. The energy dissipation rate governs the dynamics and radiation and is determined by the inflow velocity of the plasma towards the reconnection layer, $v_{\rm rec} \equiv \epsilon c$. Results from both analytical studies (Lyubarsky 2005) and PIC simulations (Guo et al. 2015; Liu et al. 2015) suggest typical values $\epsilon = 0.1 - 0.25$. For the purposes of the jet dynamics, λ, ϵ appear only through the specific combination λ/ϵ (Drenkhahn & Spruit 2002). We canonically choose $\lambda/\epsilon = 10^8$ cm (which for instance could be realized with $\lambda = 50 r_g(3M_\odot)$, $\epsilon = 0.2$). The uncertainty in this parameter can also be estimated. Given the ranges of expected values for λ and ϵ noted above, we typically expect $3 \times 10^7\,{\rm cm} \lesssim \lambda/\epsilon \lesssim 3 \times 10^9$ cm.

We consider a steady flow, characterized by a luminosity L. The flow at the Alfvén point is characterized by its magnetization parameter:

$$\sigma_0 = \frac{L_{B,0}}{L_{\rm kin,0}} = \frac{\beta_0 c (B_0 r_0)^2}{4\pi \Gamma_0 \dot{M} c^2} \quad (1)$$

where $\beta = v/c$, B_0 and Γ_0 are the magnetic field strength and bulk Lorentz factor, respectively, at the radius r_0 and $\dot{M}$ is the mass flux per sterad (all in the central engine frame).

The flow starts at r_0 with the Alfvén speed $\Gamma_0 = \sqrt{\sigma_0 + 1} \gg 1$ and accelerates as σ decreases (so we can assume $\beta \approx 1$). The total luminosity (per steradian) at this radius is the magnetic plus kinetic components:

$$L = (\sigma_0 + 1)\Gamma_0 \dot{M} c^2 \approx \sigma_0 \Gamma_0 \dot{M} c^2. \quad (2)$$

Assuming that a fraction of order unity of the dissipated energy goes towards accelerating the flow, we have that at any given radius $\sigma(r)\Gamma(r) = \sigma_0 \Gamma_0$. The acceleration is completed when $\sigma \lesssim 1$ and we get the terminal Lorentz factor (or equivalently the total energy per baryon, η) $\eta \equiv \Gamma_\infty = \Gamma_0 \sigma_0 = \sigma_0^{3/2}$. We denote the location where this happens by $r_{\rm s}$ (saturation radius). The dependence of Γ on radius for $r_0 < r < r_{\rm s}$ is derived in Drenkhahn (2002) and found to be

$$\Gamma = \Gamma_\infty \left(\frac{r}{r_{\rm s}}\right)^{1/3}, \quad (3)$$

where $r_s = \lambda\Gamma_\infty^2/(6\epsilon) = 1.7\times10^{13}\eta_3^2(\lambda/\epsilon)_8$ cm. Intuitively, r_s can be understood as the radius by which particles that were initially furthest away from the reconnection sheets finally reach the reconnection layer, where they are accelerated.

Following Giannios & Spruit (2005), we can now compute how the various flow parameters change with radius. The Poynting luminosity (per steradian) at any radius is given by

$$L_B = c\frac{(rB)^2}{4\pi} = L\left(1-\frac{\Gamma}{\Gamma_\infty}\right). \quad (4)$$

From this we obtain the energy dissipation rate, $\mathrm{d}\dot{E}$, released between r and $r+\mathrm{d}r$:

$$\mathrm{d}\dot{E} = -\frac{\mathrm{d}L_B}{\mathrm{d}r}\mathrm{d}r = \frac{0.15L}{r_{12}^{2/3}}\eta_{2.5}^{-2/3}\left(\frac{\lambda}{\epsilon}\right)_8^{-1/3}\mathrm{d}r_{12}, \quad (5)$$

where we use here and elsewhere the notation q_x for $q=10^x$ in cgs units. Therefore, $\dot{E}=\int\mathrm{d}\dot{E}\propto r^{1/3}$. We see that the energy dissipation is quite gradual and although it is dominated by the outer regions of the flow ($r\to r_s$) it could still result in a significant contribution to the emission from the photospheric radius, $r_{\rm ph}$ (to be defined below), depending on $(r_{\rm ph}/r_s)$.

$d\dot{E}$ can be related to the electron number flux (assuming an electron–proton plasma):

$$\mathrm{d}\dot{N}_e = \frac{d\dot{E}}{\xi^{-1}\Gamma\sigma m_p c^2} \quad (6)$$

where ξ is the fraction of these electrons accelerated in the reconnection sites and the denominator is the dissipated energy per accelerated particle in the flow. As with $\dot{E}$, $\dot{N}_e(r)=\int\mathrm{d}\dot{N}_e$ increases with $r^{1/3}$ (the rate of energy injection dictates the rate of particle injection). In particular, $\dot{N}_e(r_s)=\xi\dot{M}/m_p$ as required by the fact that all of the available energy is dissipated by r_s. PIC simulations suggest that ξ is of order unity, i.e. a large fraction of the electrons undergo acceleration at the current sheet (Sironi et al. 2015). We assume here a range $0.03\lesssim\xi\lesssim1$ and use $\xi\approx0.2$ as a canonical value. PIC simulations find that the accelerated electrons initially form a power-law energy spectrum (before particles can cool down due to radiation):

$$\frac{\mathrm{d}\dot{N}_e}{\mathrm{d}\gamma} = A\gamma^{-p} \quad ; \quad \gamma_i<\gamma<\gamma_f, \quad (7)$$

where p depends sensitively on σ (Sironi & Spitkovsky 2014; Guo et al. 2015; Kagan et al. 2015; Werner et al. 2016). Sironi & Spitkovsky (2014) find $p=[4,\,3,\,2,\,1.5]$ for $\sigma=[1,\,3,\,10,\,50]$ correspondingly. For numerical results, we adopt $p=4\sigma^{-0.3}$ which results in a reasonable fit for the above figures, within the relevant range of σ. The average energy per accelerated particle can now be written in terms of γ_i, γ_f, p. This energy equals a fraction $\epsilon_e/2$ of the dissipated energy per particle (since about half of the dissipated energy goes directly towards bulk acceleration; see Drenkhahn & Spruit 2002). We obtain (for $p\neq1,2$)

$$\frac{(1-p)}{(2-p)}\frac{\gamma_f^{2-p}-\gamma_i^{2-p}}{\gamma_f^{1-p}-\gamma_i^{1-p}} = \frac{\epsilon_e}{2\xi}\sigma\frac{m_p}{m_e}. \quad (8)$$

Reconnection simulations with electron–proton plasmas suggest that $\epsilon_e\approx0.2$ (Sironi et al. 2015). Equation (8) may be solved for γ_i given γ_f or vice versa. For $p<2$ (corresponding to $\sigma>10$), E_e is dominated by the highest energy particles and we can assume that $\gamma_i\approx1$ (this is also in accordance with results of PIC simulations) and solve equation (8) for γ_f. Since $\gamma_f\to\infty$ as $p\to2$, this treatment thus becomes invalid once $\gamma>\gamma_{\rm Max}$ (where $\gamma_{\rm Max}$ is the maximal synchrotron energy obtained when the time for energy loss due to synchrotron equals the acceleration time; de Jager et al. 1996). In this case, $\gamma_f=\gamma_{\rm Max}$. For $p>2$ (i.e. regions with $\sigma<10$), particles with $\gamma=\gamma_i$ dominate E_e and equation (8) simplifies to $\gamma_i=\frac{p-2}{p-1}\frac{\epsilon_e}{2\xi}\sigma\frac{m_p}{m_e}$. In this regime, we assume that $\gamma_f=\gamma_{\rm Max}$ continues to hold and solve equation (8) for γ_i (in fact γ_f quickly becomes irrelevant in this regime).

In order to determine the resulting emission from the flow, we turn to calculate the comoving magnetic field and density. Using equations (3) and (4), we obtain the comoving magnetic field,

$$B' = \frac{B}{\Gamma} = \frac{4.1\times10^6}{r_{12}^{4/3}}\frac{L_{52}^{1/2}}{\eta_3^{1/3}}\left(\frac{\lambda}{\epsilon}\right)_8^{1/3}\mathrm{G}. \quad (9)$$

The comoving density is obtained from the continuity equation $\dot{M}=r^2\Gamma\rho' c$, by plugging into equations (3) and (2),

$$\rho' = \frac{9.4\times10^{-10}}{r_{12}^{7/3}}\frac{L_{52}}{\eta_3^{4/3}}\left(\frac{\lambda}{\epsilon}\right)_8^{1/3}\mathrm{g\,cm^{-3}}. \quad (10)$$

We can relate the density to the optical depth as a function of radius by (Abramowicz, Novikov & Paczynski 1991)

$$\tau = \int_r^\infty\Gamma(1-\beta)\kappa_{\rm TS}\rho'\mathrm{d}r, \quad (11)$$

where $\kappa_{\rm TS}$ is the Thomson electron scattering opacity. The photospheric radius is the radius for which $\tau(r_{\rm ph})=1$,

$$r_{\rm ph} = 4.6\times10^{11}\left(\frac{\lambda}{\epsilon}\right)_8^{2/5}\frac{L_{52}^{3/5}}{\eta_3}\,\mathrm{cm}. \quad (12)$$

The photosphere could be pushed to larger radii if there is a significant amount of pair creation taking place at this radius. We return to this point in Section 2.2. At the photospheric radius, the Lorentz factor and magnetization are given by

$$\Gamma(r_{\rm ph}) = \Gamma_\infty\left(\frac{r_{\rm ph}}{r_s}\right)^{1/3} = 300L_{52}^{1/5}\left(\frac{\lambda}{\epsilon}\right)_8^{-1/5} \quad (13)$$

$$\sigma(r_{\rm ph}) = \eta/\Gamma(r_{\rm ph}) = 3.2\eta_3L_{52}^{-1/5}\left(\frac{\lambda}{\epsilon}\right)_8^{1/5}. \quad (14)$$

Thus, Γ is almost fixed at the photosphere and is of order 300. In addition, we see that the magnetization at the photosphere is mainly dependent on the baryon load. Finally, notice that $r_{\rm ph}<r_s$ requires

$$\eta > 290\left(\frac{\lambda}{\epsilon}\right)_8^{-1/5}L_{52}^{1/5}, \quad (15)$$

which has a weak dependence on the model parameters.

2.2 Radiation

As energy is dissipated, it is transformed into radiation. Energy is dissipated in both regions of high and low Thomson optical depths. Here, we assume that sub-photospheric dissipation is reprocessed into a quasi-thermal, blackbody emission component while synchrotron dominates at the $\tau<1$ region. In practice, neither the photospheric emission is a pure blackbody nor the optically thin emission pure synchrotron (e.g. Giannios 2006; Giannios & Spruit 2007; Beloborodov 2011; Vurm, Beloborodov & Poutanen 2011; Beloborodov 2013; Vurm & Beloborodov 2016).

The general tendency is that thermalization is achieved at large optical depths while the $\tau \ll 1$ region is dominated by synchrotron emission. However, the transition does not take place suddenly at $\tau = 1$. A full radiative transfer treatment of this problem is needed in order to properly analyse the intermediate regime. Such calculations have only been carried so far in the context of photospheric models without energy dissipation close to the photosphere (Ito et al. 2015; Lazzati 2016). This requires a more involved calculation and is beyond the scope of the current work, in which we aim to highlight the qualitative features of the model at hand. We briefly return to discuss the validity of this simplifying assumption after describing the synchrotron frequencies in the Appendix.

At small radii (below the photosphere), photons and matter are in thermodynamic equilibrium, both sharing some temperature T. As the flow propagates, the comoving temperature decreases: $T' \propto r^{-7/9}$ (Giannios & Spruit 2005). Since the thermal luminosity decreases as $L_{\rm th}(r) \propto r^2\Gamma^2T'^4 \propto r^{-4/9}$, only a fraction $(r/r_{\rm ph})^{4/9}$ of the dissipated energy at r remains thermal at the photosphere. Plugging into the energy dissipation rate, we get

$$L_{\rm ph} \propto \int_0^{r_{\rm ph}} \frac{{\rm d}r}{r^{2/3}} \left(\frac{r}{r_{\rm ph}}\right)^{4/9} = 6.6\times10^{50} L_{52}^{6/5} \left(\frac{\lambda}{\epsilon}\right)_8^{-1/5} \times \eta_3^{-1}\ {\rm erg\,s^{-1}\,sterad^{-1}}, \quad (16)$$

and the corresponding temperature is

$$T_{\rm ph} = T'_{\rm ph}\Gamma(r_{\rm ph}) = 110 L_{52}^{3/10}\eta_3^{1/4}\left(\frac{\lambda}{\epsilon}\right)_8^{-11/20}\ {\rm keV}. \quad (17)$$

The temperature at the photosphere thus naturally resides close to the observed peak of the prompt GRB emission This calculation assumes a pure blackbody spectrum. If photons are not produced efficiently enough, the temperature can get higher and a Wien Spectrum is obtained instead of a Planck spectrum (Bégué & Pe'er 2015). However, electrons accelerated due to reconnection below the photosphere may produce sufficient synchrotron photons for complete thermalization to take place. A deviation from a blackbody spectrum could also occur due to IC scatterings of the thermal photons by the relativistic electrons in the flow. This could build up a high-energy tail above the thermal peak. However, as shown in the Appendix the effective Compton Y parameter in this model is expected to be much smaller than unity, $Y \lesssim 0.01$, implying that although IC effects may distort somewhat the shape of the blackbody spectrum, their effects are energetically sub-dominant and cannot significantly change the typical temperature and flux.

For $r_{\rm ph} < r < r_{\rm s}$, matter and radiation decouple. The resulting emission is non-thermal and since the jet is highly magnetized, it will be dominated by synchrotron emission (Beniamini & Piran 2014). The properties of the emission are characterized by $\nu_{\rm syn}$, the synchrotron frequency emitted by the typical energy electrons (these are either electrons with $\gamma = \gamma_{\rm i}$ for $p > 2$ or electrons with $\gamma = \gamma_{\rm f}$ for $p < 2$), and $\nu_{\rm c}$, the synchrotron frequency emitted by electrons that cool over the dynamical time-scale,

$$\nu_{\rm syn} = \Gamma\gamma_{\rm e}^2\frac{qB'}{2\pi m_{\rm e}c} \approx 2\times10^{22}\left(\frac{r_{\rm ph}}{r}\right)^{5/3}\frac{\eta_3^3}{L_{52}^{1/2}}\left(\frac{\epsilon_{\rm e}}{\xi}\right)^2{\rm Hz} = 1.4\times10^{19}\left(\frac{r_{\rm s}}{r}\right)^{5/3}\frac{L_{52}^{1/2}}{\eta_3^2}\left(\frac{\epsilon_{\rm e}}{\xi}\right)^2\left(\frac{\lambda}{\epsilon}\right)_8^{-1}{\rm Hz} \quad (18)$$

$$\nu_{\rm c} = \frac{72\pi q m_{\rm e}c^3\Gamma^3}{\sigma_{\rm T}^2B'^3r^2} \approx 4\times10^8\left(\frac{r}{r_{\rm ph}}\right)^3\frac{L_{52}^{3/10}}{\eta_3}\left(\frac{\lambda}{\epsilon}\right)_8^{-4/5}{\rm Hz} = 10^{16}\left(\frac{r}{r_{\rm s}}\right)^3\frac{\eta_3^8}{L_{52}^{3/2}}\left(\frac{\lambda}{\epsilon}\right)_8{\rm Hz}, \quad (19)$$

where q is the electron charge and $\sigma_{\rm T}$ is the Thomson cross-section. If $\eta_3 \gtrsim 3$, then $\sigma(r_{\rm ph}) \gtrsim 10$ and $p(r_{\rm ph}) \lesssim 2$. In this case, at the photosphere, $\nu_{\rm m} = \nu(\gamma_{\rm f})$. For smaller values of η, $\nu_{\rm syn} = \nu(\gamma_{\rm i})$ (and since σ decreases with r, this remains the case up until $r_{\rm s}$). The numerical expression in equation (18) tends to overpredict the value of $\nu_{\rm syn}(r_{\rm ph})$ when $2 \lesssim \eta_3 \lesssim 6$ and the factor $((p-2)/(p-1))^2$ significantly deviates from unity. The values of $\nu_{\rm c}$ close to the photosphere, as given by equation (19), are extremely low and imply that electrons would very quickly cool down to extremely low values of $\gamma\beta \approx 1$ and below (recall that $\gamma_{\rm c}\beta_{\rm c} = \gamma_{\rm e}\beta_{\rm e}(\nu_{\rm c}/\nu_{\rm syn})^{1/2}$). In this regime, the regular synchrotron expressions do not hold any longer, and as a result, the expression for $\nu_{\rm c}$ should be modified. However, as shown below $\nu_{\rm SSA}(r_{\rm ph}) \gg \nu_{\rm c}(r_{\rm ph})$. Therefore, in any case, the synchrotron emission becomes self-absorbed for electrons with $\gamma < \gamma_{\rm SSA}$ and they do not reach $\gamma_{\rm c}$ within a dynamical time.

For $r \gtrsim r_{\rm ph}$, we obtain that $\nu_{\rm syn} \gg \nu_{\rm c}$, i.e. the synchrotron radiation is strongly in the 'fast cooling' regime (Beniamini & Piran 2014). This provides further justification to the simplifying assumption that the thermal emission and non-thermal emission are largely decoupled as particles cool via synchrotron on a time-scale much shorter than the dynamical one, whereas IC losses are suppressed due to the KN effect. Furthermore, we note that $\nu_{\rm syn}(r_{\rm ph})$ typically resides in the gamma-rays. Since $\nu_{\rm m}$ decreases with radius, while $\nu_{\rm c}$ increases with radius at an even greater pace, it is possible that $\nu_{\rm c}$ becomes larger than $\nu_{\rm m}$ before $r_{\rm s}$. This occurs for

$$\eta_3 > 1.8 L_{52}^{1/5}\left(\frac{\epsilon_{\rm e}}{\xi}\right)^{1/5}\left(\frac{\lambda}{\epsilon}\right)_8^{-1/5}. \quad (20)$$

The corresponding crossover frequency is

$$\nu = 2\times10^{18}\frac{\eta_3^{11/7}}{L_{52}^{3/14}}\left(\frac{\epsilon_{\rm e}}{\xi}\right)^{9/7}\left(\frac{\lambda}{\epsilon}\right)_8^{-2/7}{\rm Hz}. \quad (21)$$

For 'fast cooling' (which as noted above is the case for the range of radii that typically dominates the emission), the maximal synchrotron spectral luminosity (per sterad), at $\nu_{\rm c}$, is given by (Sari et al. 1998)

$$L_{\nu,\max} = \frac{m_{\rm e}c^2\sigma_T\Gamma B'N_{\rm e}}{3q} = 5\times10^{34}\frac{L_{52}^{1.3}}{\eta_3^2}\left(\frac{\xi}{0.2}\right)\left(\frac{\lambda}{\epsilon}\right)_8^{1/5} \times {\rm erg\,Hz^{-1}\,s^{-1}}, \quad (22)$$

where $N_{\rm e}$ is the number of particles in a causally connected width at a radius r (and within a solid angle of 1 sterad), $N_{\rm e} = r\dot{N}_{\rm e}(r)/(2c\Gamma^2)$. One can arrive at the same result by assuming that a factor $\epsilon_{\rm e}/2$ of the power released in the range $[r, r+{\rm d}r]$, ${\rm d}\dot{E}(r)$ is radiated via the synchrotron process at $\nu_{\rm m}$ (assuming $\nu_{\rm m} > \nu_{\rm c}$), as is indeed expected in the fast cooling regime. For other frequencies, one has

$$L_\nu = \begin{cases} L_{\nu,\max}(\nu/\nu_{\rm c})^{1/3} & \nu_{\rm c} > \nu \\ L_{\nu,\max}(\nu/\nu_{\rm c})^{-1/2} & \nu_{\rm syn} > \nu > \nu_{\rm c} \\ L_{\nu,\max}(\nu_{\rm syn}/\nu_{\rm c})^{-1/2}(\nu/\nu_{\rm syn})^{-p/2} & \nu > \nu_{\rm syn} \end{cases} \quad (23)$$

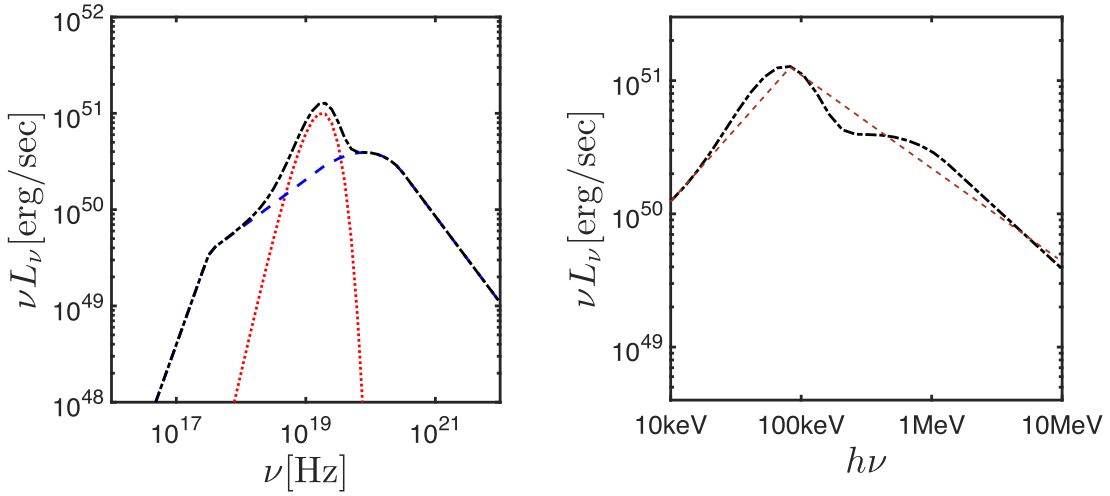

Figure 1. Spectrum obtained for $\eta_3 = 1/3$, $(\lambda/\epsilon)_8 = 4$, $L_{52} = 1$, $\xi = 0.2$. Left: the dashed line is the spectrum from the non-thermal components emitted at $r_{\rm ph} < r < r_{\rm s}$ (gradually shifting to smaller frequencies as the radius increases). A dotted line marks the narrow component (assumed for simplicity to be thermal) emitted at $r_{\rm ph}$. Finally, the dot–dashed line indicates the overall (thermal + non-thermal) spectrum. Right: close-up of the spectrum in the 10 keV to 10 MeV range (typical for prompt gamma-ray observations). The low-energy spectra approximately follows $\nu L_\nu \propto \nu^{1.1}$ whereas the high-energy part falls as $\nu L_\nu \propto \nu^{-0.7}$.

This of course holds only so long as the spectrum does not become self-absorbed, which happens for $\nu = \nu_{\rm SSA}$, where

$$\frac{2\nu_{\rm SSA}^2}{c^2}\gamma(\nu_{\rm SSA})\Gamma m_{\rm e}c^2\frac{\pi R^2}{\Gamma^2} = L_\nu(\nu_{\rm SSA}), \quad (24)$$

where $\gamma(\nu_{\rm SSA})$ is the Lorentz factor of electrons radiating synchrotron at a typical frequency $\nu_{\rm SSA}$. For typical parameters, $\nu_{\rm c} < \nu_{\rm SSA} < \nu_{\rm m}$ which using equations (23) and (24) results in

$$\nu_{\rm SSA} = 1.5\times10^{18}L_{52}^{2/15}\left(\frac{\xi}{0.2}\right)^{1/3}\left(\frac{r}{r_{\rm ph}}\right)^{-4/9}\left(\frac{\lambda}{\epsilon}\right)_8^{-7/5}\ {\rm Hz}. \quad (25)$$

Below this frequency, the spectrum becomes self-absorbed. Since the electrons are still fast cooling in this regime, the spectral slope below $\nu_{\rm SSA}$ is $F_\nu \propto \nu^{11/8}$ (Granot, Piran & Sari 2000; Granot & Sari 2002). This can naturally provide a significant reduction of the optical and X-ray fluxes, as is required in order not to overproduce the flux in these bands as compared with the upper limits from observations (Beniamini & Piran 2014). Rarer cases, in which the optical flux is apparently correlated with the gamma-rays, e.g. GRB 041219B (Vestrand et al. 2005) or GRB 080319B (Racusin et al. 2008; Beskin et al. 2010), may be the result of a combination of physical parameters (such as larger λ/ϵ, η, L or smaller ξ or distance) that corroborate to sufficiently increase $F_\nu(\nu < \nu_{\rm SSA})$. A more quantitative examination would of course require physical knowledge of the underlying parameter distributions.

The non-thermal synchrotron photons could lead to the creation of a significant amount of pairs. This leads to a cut-off in the spectrum at some frequency $\nu_{\rm co}$. Additionally, the newly formed pairs result in an increase of the particle density and hence of the photospheric radius as compared with equation (12). The optical depth for pair creation is given by

$$\tau_{\gamma\gamma}(\nu, r) = \int_r^\infty \frac{11}{180}\Gamma(1-\beta)\sigma_{\rm T}\frac{{\rm d}_L^2\int_{\nu_{\rm an}}^\infty N_\nu d\nu}{r^2\Gamma c}{\rm d}r, \quad (26)$$

where $\sigma_{\rm T}$ is the Thomson cross-section, $\nu_{\rm an} = \Gamma^2 m_{\rm e}^2c^4/(h^2\nu)$ is the frequency of a photon that can annihilate a photon with frequency ν and ${\rm d}_L^2\int_{\nu_{\rm an}}^\infty N_\nu d\nu/(r^2\Gamma c)$ is the comoving number density of annihilating photons. The pair creation cut-off frequency satisfies the condition $\tau_{\gamma\gamma}(\nu_{\rm co}) = 1$. The creation rate of positrons + electrons is then

$$\dot{N}_{\rm pairs} = 2{\rm d}_L^2\int_{\nu_{\rm co}}^\infty N_\nu d\nu. \quad (27)$$

In order to significantly change the photospheric radius, this rate must be larger than $\dot{N}$. Since the creation rate depends on the number of photons in the high-energy portion of the spectrum and the latter exponentially depends on $p(\sigma)$, one has to numerically estimate $\nu_{\rm co}$ and the change in $r_{\rm ph}$ due to pairs. For our canonical choice of parameters in this work, given in Fig. 1, $h\nu_{\rm co} \approx 500$ MeV, and the change in $r_{\rm ph}$ as compared with equation (12) is negligible.

3 RESULTS

3.1 The spectrum

The maximum angular time-scale is set at the saturation radius: $t \sim R/2c\Gamma^2 \lesssim r_{\rm s}/2c\Gamma_\infty^2 \simeq 0.1\lambda/(\epsilon c) \simeq 3\times10^{-4}(\lambda/\epsilon)_8$ s. This time is much shorter than the typical duration of a single pulse in the light curve. Therefore, within this model, any temporal behaviour in the GRB light curve directly reflects the activity of the engine. This is generic to all GRB models that involve emission from the surroundings of the photosphere. Since we are considering a continuous energy injection, this implies that the observer receives the integrated radiation emitted released between $r_{\rm ph}$ and $r_{\rm s}$.

In Fig. 1, we plot the resulting spectra obtained from a steady injection of energy into the jet. For the purposes of illustration, we assume here $\eta_3 = 1/3$, $(\lambda/\epsilon)_8 = 4$, $L_{52} = 1$, $\xi = 0.2$ and a typical redshift $z = 1$. Since σ is already quite low at the photosphere, $\sigma(r_{\rm ph}) \approx 1.3$, the emission is dominated by the thermal component, which peaks at ≈100 keV, consistent with prompt GRB observations (Kaneko et al. 2006; Nava et al. 2011). At the same location, the synchrotron emission peaks at ≈2 MeV. As the radius increases, the synchrotron emission is shifted to lower frequencies. This evolution is mainly responsible for building the high-energy spectral slope of the gamma-rays and to a lesser extent also softens somewhat the low-energy spectrum. Below ≈2 keV the emission becomes strongly suppressed due to synchrotron self-absorption.

The spectrum between ≈10 keV (typical for the low-end cut-off of gamma-ray detectors) and the peak is reasonably described by a power law: $\nu L_\nu \propto \nu^{1.1}$ (or $\alpha = -0.9$ where $N_\nu \propto \nu^{-\alpha}$ for $\nu < \nu_{\rm p}$). This is consistent with the typical values found in observations (Kaneko et al. 2006; Nava et al. 2011), which are not easily accounted for by most GRB models. The high-energy part is less smooth due to the fact that the thermal spectrum falls exponentially in this regime. On average, the spectrum between the peak frequency and 10 MeV (typical for the high-end cut-off for gamma-ray detectors) can be fitted by a power-law decline with a slope: $\nu L_\nu \propto \nu^{-0.7}$ ($\beta = -2.7$ where $N_\nu \propto \nu^{-\beta}$ for $\nu > \nu_{\rm p}$). This is consistent with observed values for some prompt GRB spectra although slightly steeper than the average value. However, due to the strong dependency of $\nu_{\rm syn}(r)$ on ξ, changing, for instance, ξ from 0.2 to 0.1 is sufficient to lead to a more typical $\beta = -2.35$. This has almost no effect on the peak frequency and also increases the low-energy spectral slope to $\alpha = -0.7$ (which is still very common).

3.2 Predictions/observables of the model

The efficiency of prompt GRBs, defined as $\eta_\gamma \equiv E_\gamma/(E_\gamma + E_{\rm kin})$ (where $E_{\rm kin}$ is the kinetic energy of the outflow before it decelerates due to interaction with the external medium), can easily be estimated within this model. For fast cooling electrons, at any given radius, $\mathrm{d}L_{\rm syn} \approx \mathrm{d}\dot{E}_{\rm e} \approx (\epsilon_{\rm e}/2)\mathrm{d}\dot{E}$ (see Section 2.2). Since $\int_{r_{\rm ph}}^{r_{\rm s}} \mathrm{d}\dot{E} \approx (1/2)L$ (the exact value in the last expression depends of course on the location of the photosphere), the total synchrotron luminosity is given by $L_{\rm syn} \approx (\epsilon_{\rm e}/4)L$. Combining this with the thermal luminosity (equation 16) gives a total efficiency of $\eta_\gamma \approx 0.1$ for the canonical parameters considered here. This is in accordance with estimates of the efficiency based on afterglow observations, suggesting that $\eta_\gamma = 0.1$–0.2 (Beniamini et al. 2015; Beniamini, Nava & Piran 2016).

The narrow photospheric component typically peaks at around a few hundred keV. This temperature is not so sensitive to the model parameters. However, the thermal luminosity (relative to the overall luminosity) decreases with η (or equivalently σ_0) and is less sensitive to the other parameters, provided that $r_{\rm s} > r_{\rm ph}$ (see below for discussion of the other limit). At the same time, the synchrotron flux changes significantly with η. At the high-energy portion of the spectrum, there are competing effects. $\nu_{\rm syn}(r_{\rm ph})$ increases with η. However, the same trend also leads to a decrease in the magnetization and the value of p. This results in more pair creation, which may become sufficient to push the photosphere outwards and decrease the typical synchrotron frequency. The most important change, however, is at the low-energy end of the spectrum (down to a few keV). This is typically controlled by $\nu_{\rm syn}(r_{\rm s})$ which decreases as η^{-2}. This leads to the observable prediction of the model according to which bursts with softer low-energy spectral slopes have a weaker thermal bump. Since p decreases with η, the non-thermal component in the spectrum of these bursts, above their peak, would also be flatter and would be observable up to larger frequencies (before cutting off at the pair-creation cut-off or at the maximal synchrotron frequency). The slope of $N_{\nu,{\rm syn}}$ above $\nu_{\rm syn}(r_{\rm ph})$ is approximately given by

$$-\frac{p(r_{\rm ph})+2}{2} = -1 - 1.4(\lambda/\epsilon)_8^{0.06}\frac{L_{52}^{0.06}}{\eta_3^{0.45}}. \quad (28)$$

For sufficiently clean jets, $\eta_3 > 1.8 L_{52}^{1/5}(\epsilon_{\rm e}/\xi)^{1/5}(\lambda/\epsilon)_8^{-1/5}$ (see equation 20), the overall spectrum becomes slow cooling before the saturation radius (and for a gradually larger extent of radii, as η increases). This results in an overall reduction of the non-thermal synchrotron luminosity. The dependence of the spectra on η described above is shown in Fig. 2 while leaving the other parameters constant at their value shown in Fig. 1.

For smaller values of η, the spectrum gradually becomes more dominated by the narrow photospheric component. As shown in Section 2.1, any material that is launched with $\eta \lesssim 290(\lambda/\epsilon)_8^{-1/5}L_{52}^{1/5}$ would lead to a completely thermal signature. This may have in fact been observed. In a recent study, Beniamini & Kumar (2016) claimed that X-ray flares must be self-absorbed between the optical and X-ray bands implying a small radius of emission and Lorentz factor for the material producing them, $R \lesssim 3 \times 10^{14}$ cm, $\Gamma \lesssim 20$. These flares could therefore arise from material that is ejected by the central engine with an initially smaller total energy per baryon. In addition, the luminosity of the thermal emission in this case is much weaker and peaks in the X-rays (Giannios & Spruit 2007). A possibly related observation is the optical transient source PTF11agg observed by the Palomar transient factory (PTF). Observations of this source favour a cosmological transient source, but fail to account for the simplest expectations from an off-axis GRB (Cenko et al. 2013). Cenko et al. (2013) argue that the most likely origin for this transient is then a 'dirty fireball', which is a burst with significantly suppressed high-energy emission, that would nonetheless still produce an afterglow as the material collides with the external medium. In the model considered in this paper, due to strong suppression of the prompt luminosity when $r_{\rm s} < r_{\rm ph}$, such a situation would naturally arise if the prompt material is ejected with low enough η.

The dependence of the model on the other three parameters λ/ϵ, L and ξ is shown in Figs 3–5. The main effect of increasing λ/ϵ is to reduce $\nu_{\rm syn}(r_{\rm ph})$, thus slightly shifting the non-thermal spectrum to lower frequencies. λ/ϵ also strongly affects the SSA frequency. When it is small, the X-ray emission is strongly suppressed by absorption, whereas larger values could lead to detectable X-ray (and possibly even optical) emission during the prompt. The dependence on L is straightforward, corresponding mainly to a linear increase in the non-thermal emission and a slightly stronger increase in the photospheric component. Finally, increasing ξ reduces both $\nu_{\rm syn}(r_{\rm ph})$ and $\nu_{\rm syn}(r_{\rm s})$, resulting in smaller effective values of α, β.

As mentioned in Section 2.1, the value of Γ at the photosphere is almost constant in this model. Since most of the emission originates from this radius (and in particular the highest energy emission), this condition can be related to the maximal frequency of a synchrotron photon that can be accounted for by this model

$$h\nu_{\rm syn,Max}(r_{\rm ph}) = 5.5 L_{52}^{1/5}\left(\frac{\lambda}{\epsilon}\right)_8^{-1/5}\ {\rm GeV} \quad (29)$$

in the central engine frame. As shown in Section 3, a cut-off in the spectrum may be seen at even lower frequencies due to pair creation. Equation (29) still provides a rough upper limit on the observable synchrotron photons in this model. Although a few higher energy photons have been observed in some bursts, it has been argued that they could originate from the external forward shock (Gao et al. 2009; Kumar & Barniol Duran 2009, 2010; Ghisellini et al. 2010).

Finally, various correlations of the type $E_{\rm p} - E_{\rm iso}$, $E_{\rm p} - E_\gamma$ or $E_{\rm p} - L_{\rm p}$ have been reported in GRB literature (Amati et al. 2002; Ghirlanda, Ghisellini & Lazzati 2004; Yonetoku et al. 2004). Typically, studies of this type have found that $E_{\rm p} \propto L_{\rm p}^{1/2-2/3}$. Assuming that the location and luminosity of the peak is dominated by the thermal component, we have $T_{\rm ph} \propto L_{\rm ph}^{1/4}(\lambda/\epsilon)^{-1/2}\eta^{1/2}$. Therefore,

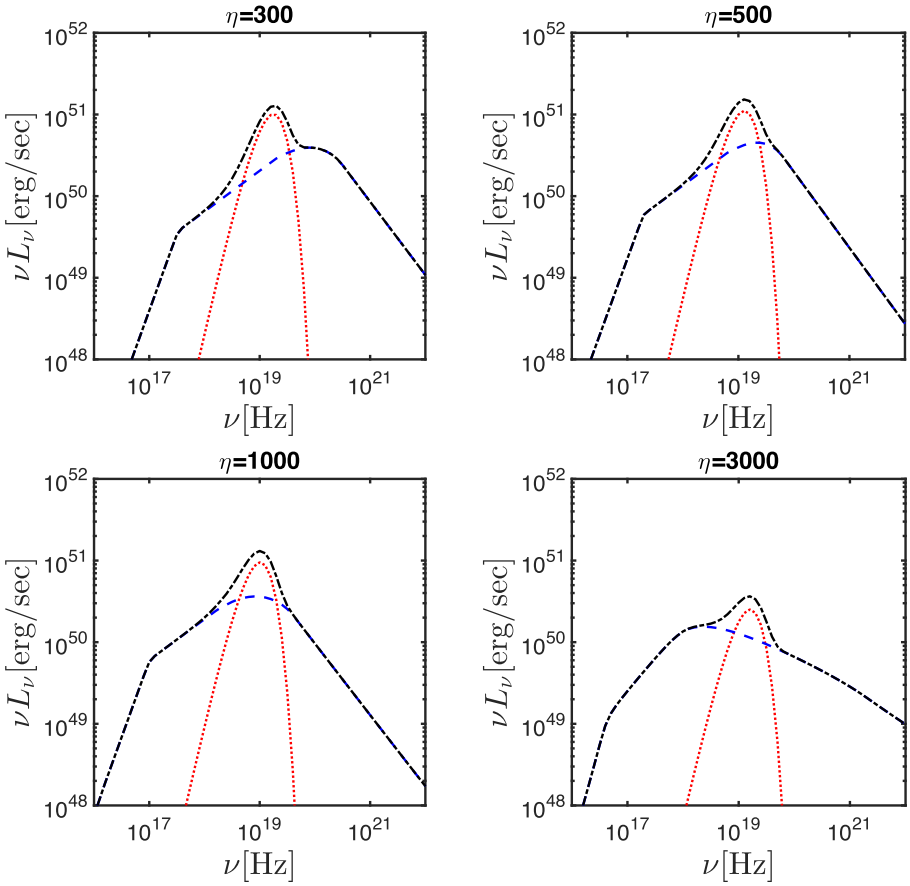

Figure 2. Spectra obtained for $(\lambda/\epsilon)_8 = 4$, $L_{52} = 1$, $\xi = 0.2$ and different values of η. Starting from top left and in the clockwise order $\eta = 0.3, 0.5, 1, 3$.

a correlation similar to the observed one can be realized if, for instance, $\eta \propto L^{\sim 1/2-5/6}$ and λ/ϵ is not strongly correlated with the other parameters (see also Giannios & Spruit 2007). Assuming this relation between η and L would imply that the above correlations would also hold for different pulses within a given burst, as was indeed observed in several cases (Guiriec et al. 2015). Furthermore, it would naturally result in an intensity tracking evolution within a given pulse (Lu et al. 2012) and in pulse widening at lower frequencies (Fenimore et al. 1995) and spectral lags (Norris et al. 1996).

4 SUMMARY

We considered a model for the prompt phase of GRB emission arising from a magnetized outflow undergoing gradual energy dissipation due to magnetic reconnection. The dissipated magnetic energy is translated to bulk kinetic energy in the jet and to acceleration of particles. The energy stored in these particles is released in the form of synchrotron radiation as they gyrate around the strong magnetic fields in the jet. At small radii, the optical depth is large, and the emission is reprocessed through Comptonization into a narrow, quasi thermal component. At larger distances the optical depth becomes small and the radiation escapes the system in non-thermal form. The overall efficiency of the radiation (as compared with the jet power) is of order 0.1, as required by afterglow observations.

The peak of the spectrum in this model is dominated by the photospheric component and is expected to reside at the sub-MeV range, as observed in prompt GRBs. Furthermore, possible correlations with the luminosity (both when comparing different pulses in a given GRB, and between different GRBs) are possible depending on the inter-relations of the model's intrinsic parameters, the jet luminosity, L, the 'wavelength' of the structured magnetic field in the jet over the outflow velocity from the reconnection sites, λ/ϵ, and the initial total energy per baryon, η. This would then also lead to an intensity tracking evolution within a given GRB pulse, to pulse widening at lower frequencies and to spectral lags, all of which have also been reported in observational prompt GRB studies. For matter ejected from the central engine with $\eta \lesssim 290(\lambda/\epsilon)_8^{-1/5} L_{52}^{1/5}$, the emission is completely thermalized. This may account for the common phenomena of X-ray flares. The temperature can be reduced to $\approx$4 keV, by assuming, for instance, $L = 10^{52}\,\mathrm{erg\,s^{-1}}(\lambda/\epsilon) = 10^8\,\mathrm{cm}$, $\eta = 20$ (Giannios & Spruit 2007). This leads to a flare luminosity which is $L = 6 \times 10^{49}\,\mathrm{erg\,s^{-1}}$ which is rather typical for a flare occurring a few hundred seconds after the trigger (Margutti et al. 2011). Due to the typically small signal-to-noise ratio, the spectra of these flares cannot be measured except for a very few cases. There is some suggestion that the brightest flares can be fitted (in the X-ray band) with a power-law spectrum: $F_\nu \propto \nu^{-1.1}$ (Chincarini et al. 2010), which would be incompatible with the expectations for the low-η material. However, the spectrum must become significantly harder at lower frequencies to be compatible with contemporaneous upper limits on the optical flux, which is suggestive of a photospheric origin (Beniamini & Kumar 2016).

The non-thermal synchrotron component leads to a softening of the spectrum below the thermal peak and to hardening of the spectrum above it. For our canonical parameters (see Section 3), we find that the low-energy spectral slope is $\alpha = -0.9$ and the high-energy spectral slope is $\beta = -2.7$. More generally, given the

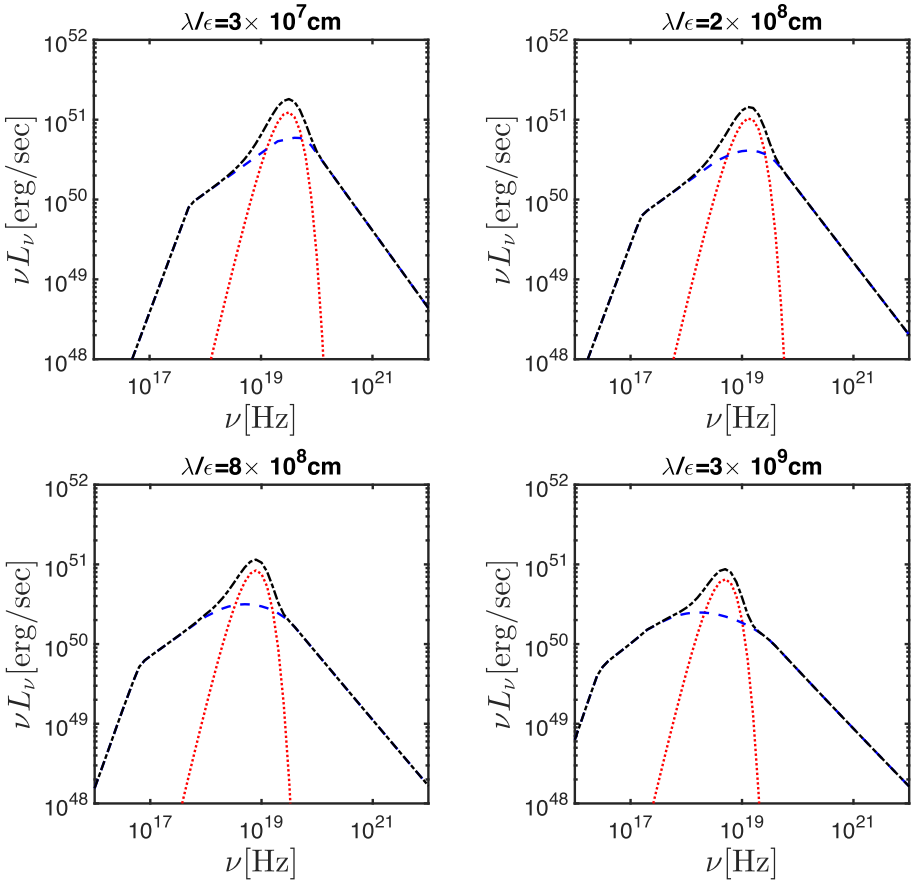

Figure 3. Spectra obtained for $\eta_3 = 1$, $L_{52} = 1$, $\xi = 0.2$ and different values of λ/ϵ. Starting from top left and in the clockwise order $\lambda/\epsilon = 3 \times 10^7$, 2×10^8, 8×10^8, 3×10^9 cm.

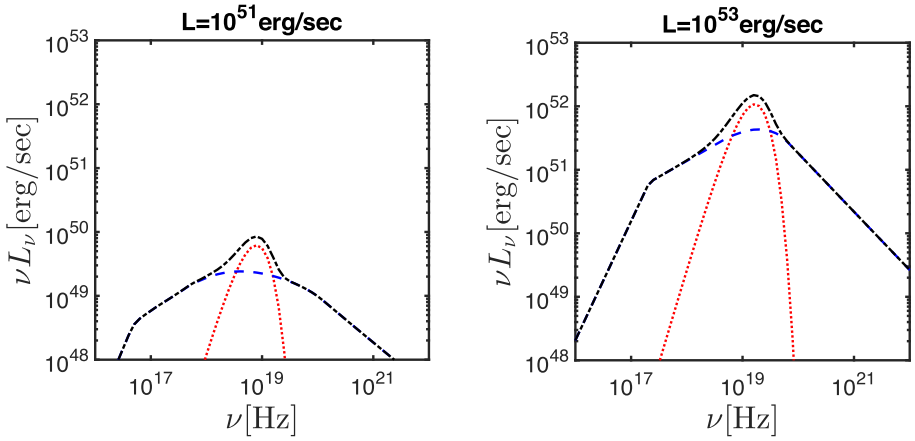

Figure 4. Spectra obtained for $\eta_3 = 1$, $(\lambda/\epsilon)_8 = 4$, $\xi = 0.2$ and different values of L. Left: $L_{52} = 0.1$; right: $L_{52} = 10$.

expected ranges of the intrinsic parameters in the model, these indices are expected to reside in the range $-1.8 \lesssim \alpha \lesssim 0$ and $-2.2 \lesssim \beta \lesssim -4.5$. Another observational test for any GRB model involving magnetically dominated jets has to do with the emitted fluxes in the optical and X-ray bands, as compared with observational upper limits. Beniamini & Piran (2014) have shown that one zone magnetic models overproduce synchrotron emission in these environments. As shown in figs 4 and 5 of Beniamini & Piran (2014), the typical radius and electrons' Lorentz factor at the photosphere in the model considered here ($r_{\rm ph} \approx 2 \times 10^{12}$ cm, $\gamma_{\rm m} \approx 10^3$) are consistent with the upper limits on the optical and X-ray fluxes from observations (this is mainly due to the spectrum being self-absorbed below a few keV). Furthermore, due to the gradual energy release in this model, a significant fraction of radiation is produced below the photosphere and re-processed to a thermal form, so the very short cooling times associated with the synchrotron process in these conditions (as compared with the dynamical one) do not imply that synchrotron dominates the peak of the emission, thus overcoming

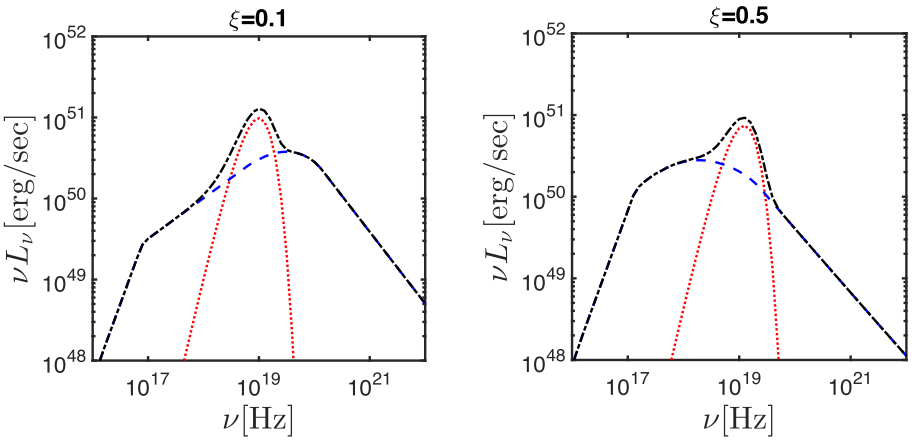

Figure 5. Spectra obtained for $\eta_3 = 1$, $(\lambda/\epsilon)_8 = 4$, $L_{52} = 1$ and different values of L. Left: $\xi = 0.1$; right: $\xi = 0.5$.

the constraints presented in Beniamini & Piran (2013, 2014) for one zone models.

The basic model presented here consists of relatively few parameters with rather narrow ranges: $0.1 \lesssim L_{52} \lesssim 10$, $300 \lesssim \eta \lesssim 3000$, 3×10^7 cm $\lesssim \lambda/\epsilon \lesssim 3 \times 10^9$ cm, $0.1 \lesssim \epsilon_e \lesssim 0.5$, $0.03 \lesssim \xi \lesssim 1$, where the latter two are informed by the latest PIC simulations. The model seems to be able to account for the basic prompt GRB observations. Simulations treating the jet dynamics, particle acceleration and radiation self-consistently are required in order to refine the model predictions. This task can, however, be much more involved and is deferred to future works.

ACKNOWLEDGEMENTS

We thank Jonathan Granot, Robert Mochkovitch, Frederic Daigne and Tsvi Piran for helpful comments and suggestions. PB is supported by a Chateaubriand fellowship.

REFERENCES

Abramowicz M. A., Novikov I. D., Paczynski B., 1991, ApJ, 369, 175
Amati L. et al., 2002, A&A, 390, 81
Axelsson M. et al., 2012, ApJ, 757, L31
Band D. et al., 1993, ApJ, 413, 281
Baring M. G., Braby M. L., 2004, ApJ, 613, 460
Bégué D., Pe'er A., 2015, ApJ, 802, 134
Bégué D., Peèr A., Lyubarsky Y., 2017, MNRAS, 467, 2594
Beloborodov A. M., 2010, MNRAS, 407, 1033
Beloborodov A. M., 2011, ApJ, 737, 68
Beloborodov A. M., 2013, ApJ, 764, 157
Beniamini P., Granot J., 2016, MNRAS, 459, 3635
Beniamini P., Kumar P., 2016, MNRAS, 457, L108
Beniamini P., Piran T., 2013, ApJ, 769, 69
Beniamini P., Piran T., 2014, MNRAS, 445, 3892
Beniamini P., Nava L., Duran R. B., Piran T., 2015, MNRAS, 454, 1073
Beniamini P., Nava L., Piran T., 2016, MNRAS, 461, 51
Beskin G., Karpov S., Bondar S., Greco G., Guarnieri A., Bartolini C., Piccioni A., 2010, ApJ, 719, L10
Burgess J. M. et al., 2011, ApJ, 741, 24
Cenko S. B. et al., 2013, ApJ, 769, 130
Cerutti B., Werner G. R., Uzdensky D. A., Begelman M. C., 2012, ApJ, 754, L33
Chincarini G. et al., 2010, MNRAS, 406, 2113
Coroniti F. V., 1990, ApJ, 349, 538
Daigne F., Bošnjak Ž., Dubus G., 2011, A&A, 526, A110
de Jager O. C., Harding A. K., Michelson P. F., Nel H. I., Nolan P. L., Sreekumar P., Thompson D. J., 1996, ApJ, 457, 253
Drenkhahn G., 2002, A&A, 387, 714
Drenkhahn G., Spruit H. C., 2002, A&A, 391, 1141
Fenimore E. E., in 't Zand J. J. M., Norris J. P., Bonnell J. T., Nemiroff R. J., 1995, ApJ, 448, L101
Gao W.-H., Mao J., Xu D., Fan Y.-Z., 2009, ApJ, 706, L33
Ghirlanda G., Celotti A., Ghisellini G., 2002, A&A, 393, 409
Ghirlanda G., Ghisellini G., Lazzati D., 2004, ApJ, 616, 331
Ghisellini G., Celotti A., 1999, ApJ, 511, L93
Ghisellini G., Tavecchio F., 2009, MNRAS, 397, 985
Ghisellini G., Ghirlanda G., Nava L., Celotti A., 2010, MNRAS, 403, 926
Giannios D., 2006, A&A, 457, 763
Giannios D., 2008, A&A, 480, 305
Giannios D., 2012, MNRAS, 422, 3092
Giannios D., Spruit H. C., 2005, A&A, 430, 1
Giannios D., Spruit H. C., 2007, A&A, 469, 1
Goodman J., 1986, ApJ, 308, L47
Granot J., 2016, ApJ, 816, L20
Granot J., Sari R., 2002, ApJ, 568, 820
Granot J., Piran T., Sari R., 2000, ApJ, 534, L163
Guiriec S. et al., 2011, ApJ, 727, L33
Guiriec S. et al., 2013, ApJ, 770, 32
Guiriec S. et al., 2015, ApJ, 807, 148
Guo F., Li H., Daughton W., Liu Y.-H., 2014, Phys. Rev. Lett., 113, 155005
Guo F., Liu Y.-H., Daughton W., Li H., 2015, ApJ, 806, 167
Ito H., Matsumoto J., Nagataki S., Warren D. C., Barkov M. V., 2015, ApJ, 814, L29
Kagan D., Sironi L., Cerutti B., Giannios D., 2015, Space Sci. Rev., 191, 545
Kagan D., Nakar E., Piran T., 2016, ApJ, 826, 221
Kaneko Y., Preece R. D., Briggs M. S., Paciesas W. S., Meegan C. A., Band D. L., 2006, ApJS, 166, 298
Katz J. I., 1994, ApJ, 432, L107
Kawanaka N., Piran T., Krolik J. H., 2013, ApJ, 766, 31
Kumar P., Barniol Duran R., 2009, MNRAS, 400, L75
Kumar P., Barniol Duran R., 2010, MNRAS, 409, 226
Kumar P., McMahon E., 2008, MNRAS, 384, 33
Lazzati D., 2016, ApJ, 829, 76
Lazzati D., Begelman M. C., 2010, ApJ, 725, 1137
Leng M., Giannios D., 2014, MNRAS, 445, L1
Liu Y.-H., Guo F., Daughton W., Li H., Hesse M., 2015, Phys. Rev. Lett., 114, 095002

Lloyd-Ronning N. M., Fryer C. L., 2016, preprint (arXiv:e-prints)
Lu R.-J., Wei J.-J., Liang E.-W., Zhang B.-B., Lü H.-J., Lü L.-Z., Lei W.-H., Zhang B., 2012, ApJ, 756, 112
Lyubarsky Y. E., 2005, MNRAS, 358, 113
Mallozzi R. S., Paciesas W. S., Pendleton G. N., Briggs M. S., Preece R. D., Meegan C. A., Fishman G. J., 1995, ApJ, 454, 597
Margutti R., Bernardini G., Barniol Duran R., Guidorzi C., Shen R. F., Chincarini G., 2011, MNRAS, 410, 1064
McKinney J. C., Uzdensky D. A., 2012, MNRAS, 419, 573
Melzani M., Walder R., Folini D., Winisdoerffer C., Favre J. M., 2014, A&A, 570, A112
Mészáros P., Rees M. J., 2000, ApJ, 530, 292
Nava L., Ghirlanda G., Ghisellini G., Celotti A., 2011, A&A, 530, A21
Norris J. P., Nemiroff R. J., Bonnell J. T., Scargle J. D., Kouveliotou C., Paciesas W. S., Meegan C. A., Fishman G. J., 1996, ApJ, 459, 393
Parfrey K., Giannios D., Beloborodov A. M., 2015, MNRAS, 446, L61
Preece R. D., Briggs M. S., Mallozzi R. S., Pendleton G. N., Paciesas W. S., Band D. L., 1998, ApJ, 506, L23
Preece R. D., Briggs M. S., Mallozzi R. S., Pendleton G. N., Paciesas W. S., Band D. L., 2000, ApJS, 126, 19
Racusin J. L. et al., 2008, Nature, 455, 183
Rees M. J., Meszaros P., 1994, ApJ, 430, L93
Ryde F., Pe'er A., 2009, ApJ, 702, 1211
Ryde F. et al., 2010, ApJ, 709, L172
Sari R., Narayan R., Piran T., 1996, ApJ, 473, 204
Sari R., Piran T., Narayan R., 1998, ApJ, 497, L17
Schaefer B. E., 2003, ApJ, 583, L71
Shahmoradi A., Nemiroff R. J., 2010, MNRAS, 407, 2075
Sironi L., Spitkovsky A., 2014, ApJ, 783, L21
Sironi L., Petropoulou M., Giannios D., 2015, MNRAS, 450, 183
Sironi L., Giannios D., Petropoulou M., 2016, MNRAS, 462, 48
Spruit H. C., Daigne F., Drenkhahn G., 2001, A&A, 369, 694
Thompson C., 1994, MNRAS, 270, 480
Vestrand W. T. et al., 2005, Nature, 435, 178
Vurm I., Beloborodov A. M., 2016, ApJ, 831, 175
Vurm I., Beloborodov A. M., Poutanen J., 2011, ApJ, 738, 77
Vurm I., Lyubarsky Y., Piran T., 2013, ApJ, 764, 143
Werner G. R., Uzdensky D. A., Cerutti B., Nalewajko K., Begelman M. C., 2016, ApJ, 816, L8
Yonetoku D., Murakami T., Nakamura T., Yamazaki R., Inoue A. K., Ioka K., 2004, ApJ, 609, 935
Yu H.-F., van Eerten H. J., Greiner J., Sari R., Bhat P. N., Kienlin A. v., Paciesas W. S., Preece R. D., 2016, J. Astron. Space Sci., 33, 109
Zhang B., Yan H., 2011, ApJ, 726, 90

APPENDIX: APPROXIMATE ESTIMATE OF COMPTONIZATION EFFECTS

Inverse Compton of the initially thermal (blackbody) photon spectrum produced below the photosphere by relativistic electrons accelerated in the reconnection sites can lead to a modification of the blackbody spectrum in a process known as Comptonization. The importance of Comptonization effects can be gauged by estimating the effective Compton Y parameter that is felt by the incident photons. As we are interested in providing an upper limit on the effectiveness of Comptonization, we can safely assume that IC takes place in the Thomson regime and neglect KN effects, which could only reduce the optical depth and energy transfer by IC (and hence the effective Compton parameter).

Since electrons are fast cooling due to synchrotron ($\gamma_{\rm c} < \gamma_{\rm m}$), the evolved energy spectrum of the electrons at a given radius is

$$\frac{{\rm d}n}{{\rm d}\gamma} \propto \begin{cases} \gamma^{-2}, & \gamma_{\rm c} < \gamma < \gamma_{\rm m} \\ \gamma^{-p-1}, & \gamma_{\rm m} < \gamma \end{cases}. \tag{A1}$$

The Y parameter is given by

$$Y(r) = \frac{4}{3}\tau_{\rm IC}\langle\gamma^2\rangle, \tag{A2}$$

where

$$\langle\gamma^2\rangle = \frac{\int_{\gamma_{\rm c}}^{\infty}\frac{{\rm d}n}{{\rm d}\gamma}\gamma^2{\rm d}\gamma}{\int_{\gamma_{\rm c}}^{\infty}\frac{{\rm d}n}{{\rm d}\gamma}{\rm d}\gamma} \approx \gamma_{\rm m}\gamma_{\rm c}\frac{p-1}{p-2} \tag{A3}$$

and $\tau_{\rm IC}$ is the optical depth for IC scatterings and is given by

$$\tau_{\rm IC} = \int_r^{\infty}\Gamma(1-\beta)\sigma_{\rm TS}n'_{\rm e}{\rm d}r \approx \frac{\xi\sigma_{\rm T}\dot{M}}{m_{\rm p}rc\Gamma^2}\left(\frac{r}{r_{\rm s}}\right)^{1/3}, \tag{A4}$$

where $n'_{\rm e}(r)$ is the number of accelerated electrons up to the radius r (in the comoving frame). Putting everything together, we find

$$Y(r) = 0.01\left(\frac{r}{r_{\rm ph}}\right)^{2/3}\eta_3^{-4/3}\left(\frac{\lambda}{\epsilon}\right)_8^{-2/3}\left(\frac{\epsilon_{\rm e}}{0.2}\right). \tag{A5}$$

We find that $Y(r) \ll 1$ for $r < r_{\rm ph}$. Comptonization effects are therefore expected to be energetically sub-dominant and cannot significantly change the typical temperature and flux. Numerical simulations are required to gain an accurate estimate of the actual spectrum above the thermal peak and are deferred to a future work. The physical situation is very different if one assumes that the dissipated energy smoothly and continuously heats *all* the electrons in the flow. In that case the Compton parameter is $Y \sim 1$ for $\tau \sim 1$ and the Compton spectral distortion is pronounced (Giannios 2006, 2008).

It should be noted that depending on the model parameters it is possible to formally have $\gamma_{\rm m}\gamma_{\rm c} < 1$. In this case, the typical Lorentz factor of the scattering electrons cannot be obtained from equation (A3). However, we note that this does not change significantly the estimate of $Y(r)$ given by equation (A5). The reason for this is that since ${\rm d}n/{\rm d}\gamma \propto \gamma^{-2}$ for $\gamma < \gamma_{\rm m}$ and $Y \propto \int\gamma^2{\rm d}n/{\rm d}\gamma{\rm d}\gamma$, we see that different logarithmic bins of γ up to $\gamma_{\rm m}$ all contribute roughly equally to the overall Compton parameter. Therefore, electrons with $\gamma_{\rm m}$ contribute roughly the same as those, for instance, with $\gamma = \sqrt{\gamma_{\rm m}\gamma_{\rm c}}$, and we do not rely on the latter to obtain the result in equation (A5). Stating it differently, the density of electrons with a Lorentz factor of order $\gamma_{\rm m}$ is smaller than the total number of accelerated electrons by the ratio of their cooling time to the dynamical time-scale

$$n'_{\rm e}(\gamma_{\rm m}) \approx \left.\frac{{\rm d}n}{{\rm d}\gamma}\right|_{\gamma_{\rm m}}\gamma_{\rm m} \approx n'_{\rm e}\frac{t_{\rm c}(\gamma_{\rm m})}{t} = n'_{\rm e}\frac{\gamma_{\rm c}}{\gamma_{\rm m}}. \tag{A6}$$

Therefore, the effective optical depth for IC scatterings with these electrons is reduced by a factor $\gamma_{\rm c}/\gamma_{\rm m}$ as compared with equation (A4). At the same time, their Lorentz factor squared is simply $\gamma_{\rm m}^2$ which is a factor $\gamma_{\rm m}/\gamma_{\rm c}$ larger than the value in equation (A3). Taking the product of the two, it is clear that τ remains unchanged and is independent of the actual value of the Lorentz factor for cooled electrons, so long as the electrons are strongly fast cooling.

This paper has been typeset from a TEX/LATEX file prepared by the author.